

HOT MWIR TECHNOLOGY AT SCD

P.C.Klipstein¹, E. Armon¹, E. Avnon¹, Y. Benny¹, M. Brumer¹, Y. Cohen¹, N. Fraenkel¹,
S. Gliksman¹, A. Glozman¹, N. Hadari¹, I. Hirsh¹, M. Katz², O. Klin¹, L. Langof¹,
I. Lukomsky¹, I. Marderfeld¹, H. Nahor¹, M. Nitzani¹, D. Rakhmilevich¹, S. Schusterman²,
I. Shafir³, I. Shtrichman¹, L. Shkedy¹, N. Sicron², N. Snapi¹, and N. Yaron¹.

¹ SemiConductor Devices P.O. Box 2250, Haifa 31021, Israel

²The Israel Center for Advanced Photonics, Yavne 81800, Israel

³Solid State Physics Department, Applied Physics Division, Soreq NRC, Yavne 81800, Israel

ABSTRACT

SCD is a leading manufacturer of MWIR InSb Focal Plane Arrays (FPA) with formats up to 3 megapixels. Using photodiode layers grown by Molecular Beam Epitaxy (MBE), the operating temperature is raised to ~ 100 K, compared with 80 K for our legacy implanted junction technology. Due to the excellent manufacturability of III-V MBE materials, we have extended this approach in the development of our newer High Operating Temperature (HOT) MWIR technologies, all of which are based on XB n and XB p barrier devices which suppress the dark current generated by traps in the depletion layer. As a result we now produce a family of InAsSb XB n FPAs operating at 150 K with a cut-off wavelength of $\lambda_C = 4.2 \mu\text{m}$. Formats range between 0.33 megapixels and 5.24 megapixels and our latest "Crane" FPA has a pitch of just $5 \mu\text{m}$. These detectors are ideal for 24/7 surveillance and long-range applications, due to large formats, increased HOT cooler reliability and very high atmospheric transmission. For applications requiring HOT full MWIR (HFMW) performance ($\lambda_C = \sim 4.9 \mu\text{m}$), we have explored three approaches, all of which have produced operating temperatures in the range 115-125 K with high FPA operability and uniformity. Using a suitable design of buffer layer, we have extended the InAsSb XB n cut-off wavelength while maintaining a high quantum efficiency above 70%. Comparable performance has also been obtained in two lattice matched type II superlattice (T2SL) architectures: XB n InAs/InAsSb and XB p InAs/GaSb. The three technologies give great flexibility in design optimization, and initial production of HFMW detectors is scheduled for mid 2022.

Keywords: XB n , XB p , MWIR, type II superlattice, photodetector

1. INTRODUCTION

The mid-wave infrared (MWIR) transparency window of the atmosphere is very important for a number of critical imaging applications. The shorter wavelength of this window compared with the long-wave infrared (LWIR) window enables greater diffraction limited resolution, while the stronger variation of the black-body (BB) radiation curve with temperature provides higher sensitivity. The MWIR window is one of the most transparent in the atmosphere, and the BB intensity at ambient temperatures is sufficiently high to allow a long imaging range with a reasonably high frame rate. The larger photon energy can also lead to lower dark currents and higher detector operating temperatures.

The maximum operating temperature for background limited performance (BLIP) can be defined as the temperature at which the photocurrent and dark current are equal. In photodiode detectors made from III-V materials such as InSb, the main source of dark current is generation in the depletion region due to Shockley-Read-Hall (SRH) generation-recombination (GR) centers [1, 2]. By preparing very high quality p - n junctions using modern molecular beam epitaxy (MBE) growth techniques the number of traps can be reduced to below one part per billion and the operating temperature raised to about 100 K. However, in order to increase the operating temperature further, the GR current must be suppressed and this has been achieved in recent years by the incorporation of a barrier layer, which both blocks the majority carriers and excludes the depletion region from the narrow band gap photon absorbing active layer (AL). The dark current is then diffusion limited and

E-mail: philip_k@scd.co.il

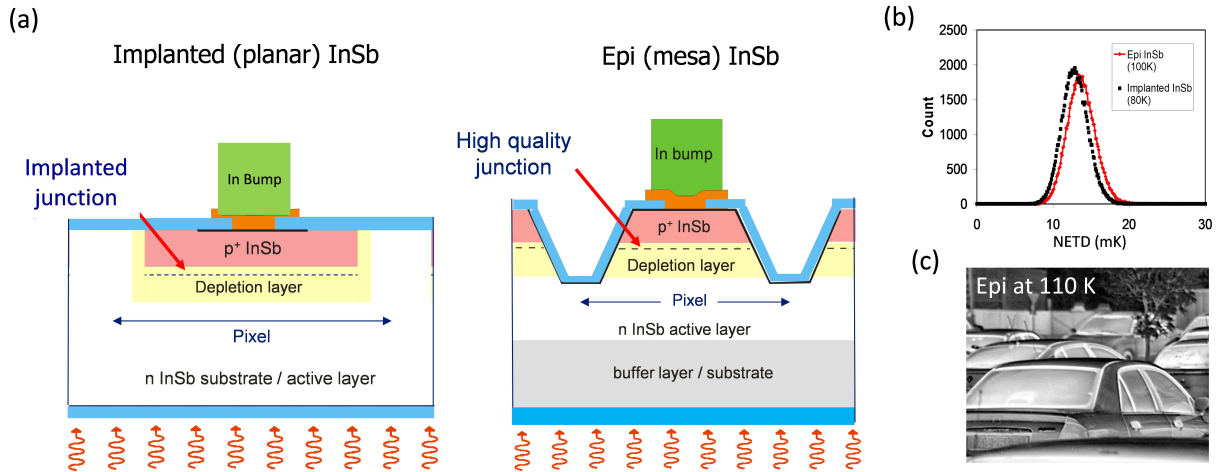


Figure 1. (a) Pixel architectures for implanted and MBE grown InSb photodiodes, (b) comparison of NETD histograms in both architectures, and (c) image registered at 110K in an MBE grown InSb FPA.

can be reduced to a level comparable with that in the equivalent II-VI device based on a mercury cadmium telluride photodiode [3]. III-V materials can be grown on commercially available substrates and present many manufacturing advantages. In this work we report on the progress of MWIR technology at SCD, comparing both photodiode and barrier devices. The photodiodes use either ion-implanted or MBE grown $p-n$ junctions in InSb, while the barrier devices are based both on bulk InAsSb and various type II superlattice (T2SL) materials. InAsSb can be grown lattice matched to a GaSb substrate or to a buffer layer that allows a larger lattice parameter to be used when longer cut-off wavelengths are required. In the second case the lack of a lattice matched substrate can be avoided by growing a T2SL. The choice of layer widths in a T2SL period enables a wide range of cut-off wavelength tunability across the whole of the MWIR range.

2. INDIUM ANTIMONIDE PHOTODIODES

Figure 1(a) compares architectures for implanted and MBE grown InSb photodiodes. Focal plane array (FPA) detectors based on the implanted device operating at 80K have been manufactured at SCD for over twenty five years with formats steadily increasing from 128×128 with a $40 \mu\text{m}$ pitch in 1995 to 1920×1536 with a $10 \mu\text{m}$ pitch today. An advantage of the implanted device is its planar architecture which simplifies the manufacturing process quite significantly, leading to very good uniformity and very high scalability and pixel operability. According to Donald Reago these attributes have made InSb planar arrays the “champion” in applications where the size and power of the cooler is acceptable [4]. Nevertheless a reduction in size, weight and power (SWaP) is an important enabler for many other applications and this has inspired SCD to develop the epi-InSb detector described in the introduction, which operates close to 100K. Figure 1(b) demonstrates that the noise equivalent temperature difference (NETD) distribution of the epi-InSb detector at 100K is very similar to that of the implanted InSb detector at 80K. This allows a clear image to be registered at 110K, which is close to the BLIP temperature of the epi-InSb detector, as shown in Figure 1(c). Figure 1(a) demonstrates that the main difference between the two architectures is pixel delineation, which requires mesa etching in the case of the epi-InSb, in order to isolate devices. Both architectures have a GR limited dark current, depicted schematically on an Arrhenius plot in Figure 2, where the characteristic GR activation energy is half the AL band gap [3]. In order to raise the operating temperature further, the GR current must be eliminated. This can be realized by the introduction of a barrier layer (BL) next to the AL, which has the same doping polarity and a much larger band gap.

3. INDIUM ARSENIDE ANTIMONIDE BARRIER DETECTORS

Two examples of the band profile of a barrier detector at operating bias are shown in Figure 2(a). A special feature of the BL is that it blocks majority carriers but allows minority carriers from the AL to flow freely. In Figure 2(a) it should be noted that the AL and BL are identical, and only the contact layer is different. This is

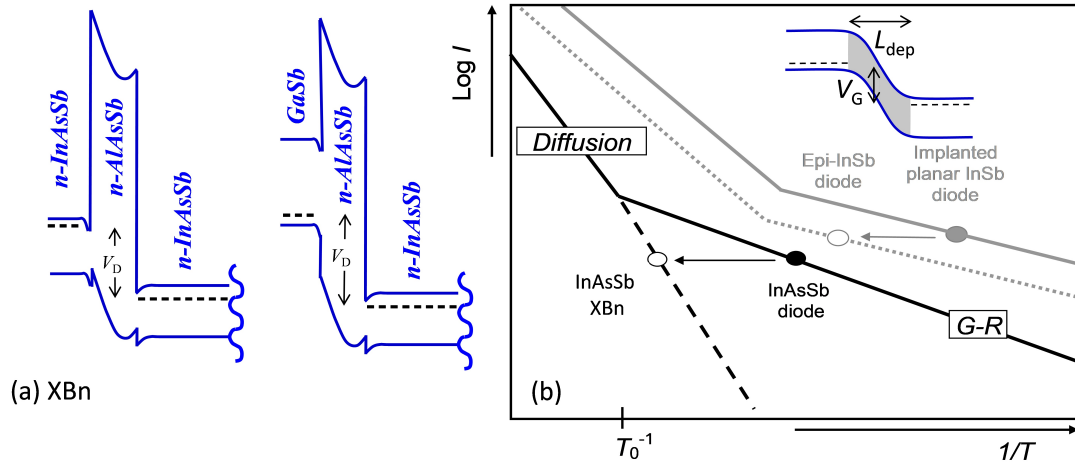


Figure 2. (a) Band profiles at operating bias for two XBn architectures (note that only the CL changes) and (b) schematic Arrhenius plots showing “diffusion” and “generation-recombination” regimes for InSb photodiodes and comparing an InAsSb photodiode with an XBn device, both grown lattice matched to the same substrate material. *Inset*: Photodiode band profile at operating bias with the depletion region shaded in gray.

true of all members of the XBn detector family based on a given photon absorbing material, where “n” stands for the AL and BL doping, “B” stands for BL and “X” represents the CL which can take several different forms. For the examples shown in the Figure, “X” stands for n-type InAsSb or p-type GaSb. These examples are by no means exhaustive and several other choices exist as discussed in Ref. [3]. In principle, all architectures exhibit the same diffusion limited dark current but their operating bias values vary because they depend on the valence band band offset of the CL, and for an n-type CL, also on the CL band gap.

Figure 3 compares the dark current in two nBn devices with a cut-off wavelength of 4.2 μm, that correspond

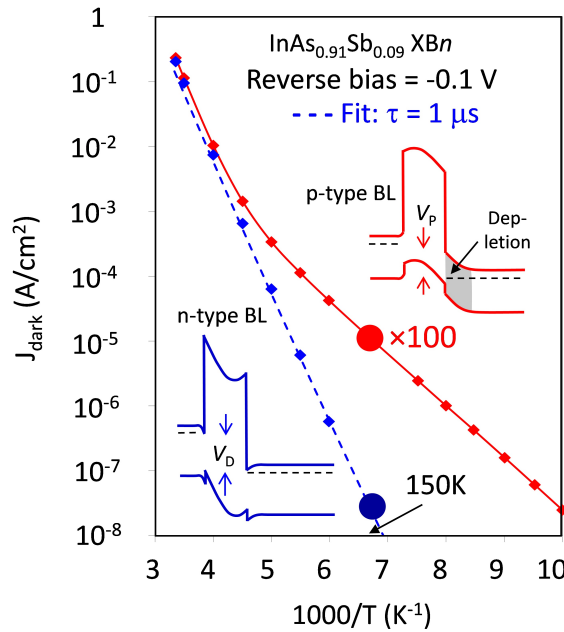


Figure 3. Arrhenius plots for two XBn devices grown lattice matched to GaSb at an operating bias of 0.1 V, as depicted in the insets, one with an n-type BL (blue) and one with a p-type BL (red). *Points*: measured values, *dashed curve*: fit to the Shockley diffusion current formula with a minority carrier lifetime of 1 μs, *solid curve*: guide for the eye.



Figure 4. Image at an FPA temperature of 150 K from SCD's XBn 2560 × 2048 / 5 μm pitch Crane detector.

to the left hand diagram in Figure 2(a). They are based on an $\text{InAs}_{0.91}\text{Sb}_{0.09}$ AL and a $\text{AlSb}_{0.91}\text{As}_{0.09}$ BL, both lattice matched to a GaSb substrate. The blue points are for an n -type BL while the red points are for nominally the same device except that the BL is not intentionally doped (*nid*) due to a failure of the doping shutter to open during BL growth. In the second case, the two slope behavior shows clearly that the *nid* BL is p -type which leads to depletion of the AL, as shown by the gray shading in the upper inset. The lower slope is due to activation by half the AL band gap corresponding to GR behavior, while the higher slope is for the full band gap and corresponds to a diffusion limited current [3]. The p -type doping is thought to arise from natural stoichiometric defects [5, 6, 7]. When the dark current in Figure 3 is compared with the typical photocurrent of the devices, the BLIP temperatures are found to be approximately 175 K for the n -type BL and 140 K for the p -type BL [3]. This shows the importance of doping the BL n -type because it leads to a higher operating temperature. The operating temperature is chosen to give a dark current which is more than one order of magnitude lower than the BLIP value so that it is essentially negligible. The operating temperature of our detectors is therefore set to 150 K, for which the dark current in Figure 3 is 100 times smaller than for a detector with a p -type BL.

The lattice matched $\text{InAs}_{0.91}\text{Sb}_{0.09}$ XBn technology is now relatively mature, with pixel operabilities above 99.8%, pixel dimensions down to 5 μm, and formats up to 2560 × 2048 [8]. An example of SCD's new 5.24 megapixel, 5 μm pitch Crane detector is shown in Figure 4. The excellent resolution obtained from such a large format can be seen quite clearly. Note also that the upper MWIR window of the atmosphere is almost perfectly matched to the wavelength range of the lattice matched XBn technology. This window is one of the most transparent atmospheric windows, so that detectors of this type have a very long range, as demonstrated by the arrow marking a distance of about 40 Km.

In order to increase the cut-off wavelength for the InAsSb XBn architecture, we have looked into the growth of buffer layers to accommodate the lattice mismatch between the device layers and the substrate. This has met with some success although it can result in significant degradation of the image quality at the FPA level. Figure 5 shows an example of the dark current density as a function of bias and temperature for such a device with a cut-off wavelength of 4.9 μm. The characteristics in Figure 5(a) show a dark current plateau close to a reverse bias of -0.6 V. This is the operating point of the devices where the dark current is diffusion limited and depends only weakly on the bias voltage. The measured dark current density at this bias is presented as points on an Arrhenius plot in Figure 5(b) where it is shown to provide a good fit to the Shockley diffusion formula, plotted as a solid line, for the band gap temperature dependence shown in the inset and a minority carrier lifetime of 110 ns. The effective densities of states of the conduction and valence bands, N_C and N_V , are calculated using an electron effective mass of $0.015m_0$, and Luttinger parameters ($\gamma_1, \gamma_2, \gamma_3$) of (30.67, 13.96, 14.86) respectively, based on the method described in Ref. [9]. The lifetime may be compared with the value of 1.0 μs determined in

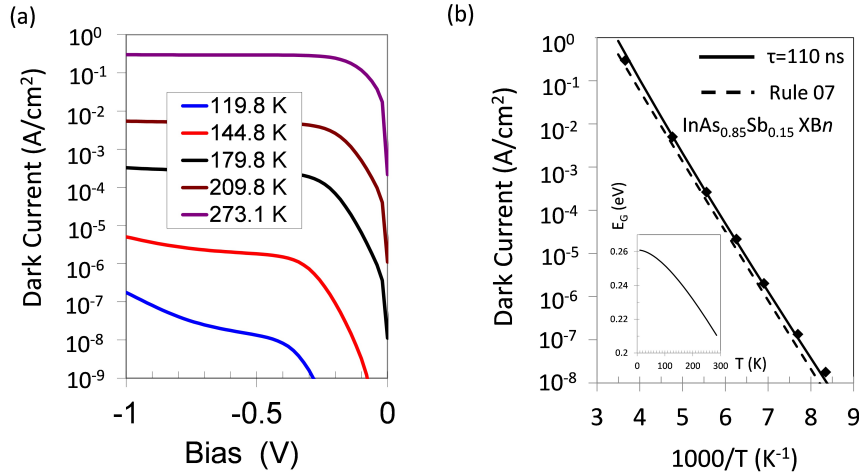


Figure 5. (a) Dark current density as a function of bias and temperature and (b) Arrhenius plot at a bias of -0.6 V for an InAs_{0.85}Sb_{0.15} XBn test device with a mesa area of $300 \times 300 \mu\text{m}^2$

a similar way by a fit to the blue points in Figure 3. In the present case the AL electron concentration is only slightly larger, by a factor of approximately two, so the nine fold reduction in lifetime is attributed mainly to the lattice mismatch which leads to a significantly higher density of SRH traps. In both cases the dark current is almost identical to the Rule 07 value for mercury cadmium telluride (MCT) which is plotted explicitly in Figure 5(b) [10]. The average quantum efficiency (QE) over the full MWIR spectral band for an FPA made from this material and with an anti-reflection coating (ARC) is close to 70%. The main challenge in this case is image quality, free from speckle or cross hatch patterns.

4. T2SL BARRIER DETECTORS

4.1 InAs/GaSb XBp and XBn devices

T2SLs offer the most direct route for extending the cut-off wavelength while maintaining a good lattice match with the substrate. We have investigated two different superlattice structures for the AL, namely InAs/GaSb and InAs/InAs_{1-x}Sb_x which both grow lattice matched to GaSb with high quality. The quality can be monitored by the width of the zero order X-ray diffraction line width which is about one order of magnitude narrower than for the non-lattice matched InAsSb layer discussed in the previous section. Figure 6 shows the dark current and QE for an InAs/GaSb T2SL XBp device with a low temperature cut-off wavelength of $5.0 \mu\text{m}$. The band profile at operating bias is depicted schematically in Figure 6(a) where the BL is an InAs/AlSb T2SL which presents a barrier in the valence band (VB) that is larger than the AL band gap, and a conduction band edge that is closely aligned with that of the AL. The operating bias is that where the QE goes into saturation, which is 0.5 V according to Figure 6(d). It also corresponds to the bias at which the dark current exhibits a plateau with only a weak dependence on bias, as discussed in the previous section. The dark current characteristics are shown for various temperatures on bias, in Figure 6(b). At 0.5 V and 118 K the dark current density is close to the operating value for the epi-InSb device discussed in Section 2, so the operating temperature is close to this temperature. The QE at 130 K without an anti-reflection coating (ARC) and averaged over the spectral range 3.2 - $3.6 \mu\text{m}$ in Figure 6(d) is 45%, while the average value for the full MWIR band with an ARC is above 50%. Figure 6(c) shows an Arrhenius plot of the dark current and a fit to the Shockley equation with a lifetime of 40 ns. The values of N_C and N_V used in the fit are calculated from an 8 band $\mathbf{k} \cdot \mathbf{p}$ model as described in Ref. [11]. This model has also been used to estimate the absorption spectrum, from which a fit to the QE at 130 K yields a vertical diffusion length of $3.5 \mu\text{m}$. The corresponding mobility, determined from the diffusion length and lifetime using the Einstein relation, is then about $300 \text{ cm}^2/\text{Vs}$. This is more than one order of magnitude lower than for similar LWIR devices reported previously [12], suggesting that mechanisms such as interface roughness scattering (IRS) may play an important role. The electrons have a large amplitude in the InAs layers which are about 50% thinner in the MWIR structure, and IRS is expected to vary as the inverse cube of the layer thickness. Thus,

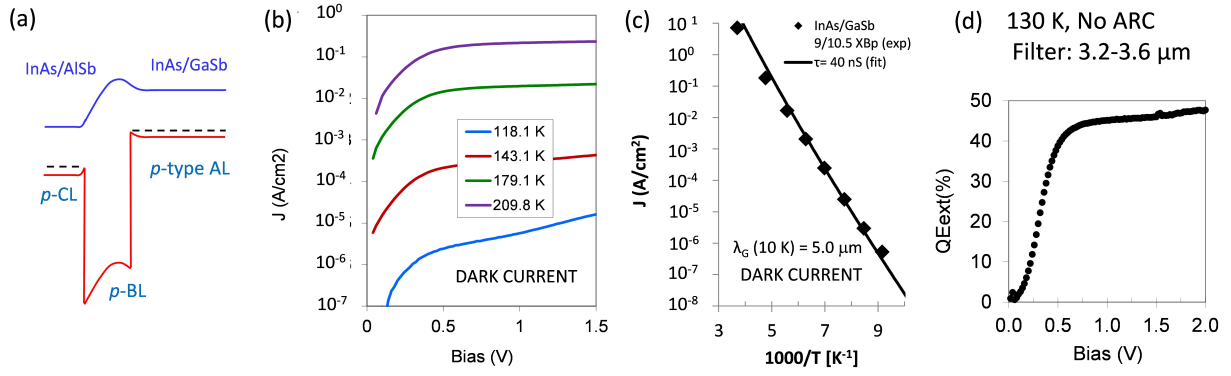


Figure 6. (a) Band profile at operating bias for a T2SL XB p device with an InAs/GaSb AL and CL and an InAs/AlSb BL, (b) dark current density as a function of bias and temperature, (c) Arrhenius plot at operating bias of 0.5 V with a fit to the Shockley diffusion equation for a minority carrier lifetime of 40 ns, and (d) QE of a $150 \times 150 \mu\text{m}^2$ test device as a function of bias at 130 K.

it seems likely that the scattering can be reduced by further adjustments to the T2SL period and AL doping, which could lead ultimately to an increase in the diffusion length and QE.

We have also investigated XB n structures based on an InAs/GaSb AL. The lifetime is similar to the XB p case but the mobility is about one order of magnitude smaller. This leads to a sub-micron diffusion length and a low QE of below 25% which is a serious limitation [12].

4.2 InAs/InAsSb XB n devices

In order to overcome the limitation of a very short lifetime in InAs/GaSb T2SL materials Steenbergen *et al.* proposed using a gallium free T2SL [13], where lifetimes as long as $10 \mu\text{s}$ have been reported [14, 15]. The absence of a good hole barrier means that barrier devices based on gallium free superlattices use an XB n architecture. Figures 7(a) and (b) show the dark current as a function of bias and temperature for two InAs/InAs $_{0.61}$ Sb $_{0.39}$ XB n devices with an AlSb $_{0.91}$ As $_{0.09}$ BL and an AL cut-off wavelength close to $5.5 \mu\text{m}$ at 120 K. In one case the AL doping, measured by capacitance-voltage profiling [16], was $9 \times 10^{15} \text{cm}^{-3}$ while in the other it was $4 \times 10^{14} \text{cm}^{-3}$. The dark current characteristics for the two samples shown in Figure 7(a) are fairly similar, with a slightly higher current at 120 K for the device with the lower doping. In contrast, the lifetimes deduced from the Arrhenius plot

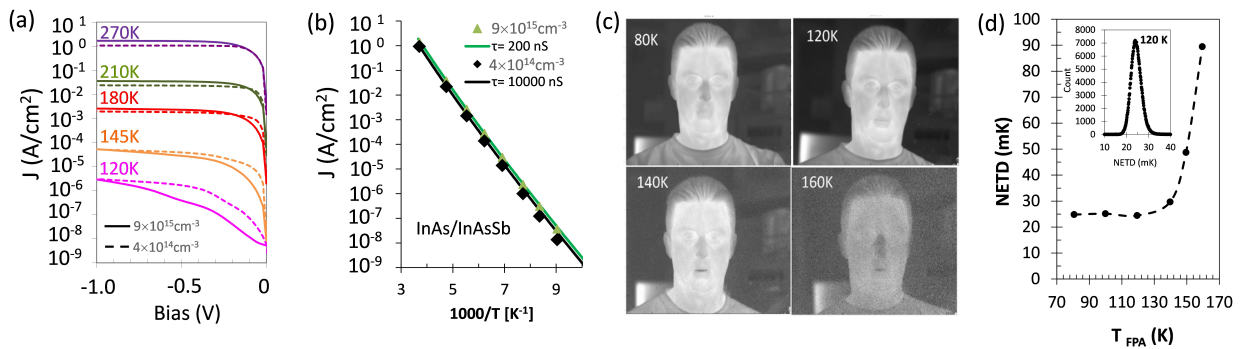


Figure 7. (a) Dark current density as a function of temperature and bias for two InAs/InAs $_{0.61}$ Sb $_{0.39}$ T2SL XB n test devices of area $300 \times 300 \mu\text{m}^2$ with the doping levels indicated in the legend, and (b) Arrhenius plots at operating bias of -0.5 V with fits to the Shockley diffusion equation for the minority carrier lifetimes indicated in the legend. (c) $15 \mu\text{m}$ pitch FPA images for the low doped material for which the temperature dependence of the NETD at 50% well fill and a BB temperature of 53 C is shown in (d) . *Inset*: NETD distribution at 120 K.

of the dark current at the operating bias of 0.5 V are very different, with values in Figure 7(b) of approximately 200 ns for high doping and 10 μ s for low doping. This strong dependence on doping has been attributed to an Auger mechanism which becomes significant for doping levels above $\sim 10^{15} \text{ cm}^{-3}$ [15]. Figure 7(c) shows images at different operating temperatures for an FPA made from the low doped material and which includes an ARC. The corresponding noise equivalent temperature difference (NETD) at 120 K, measured at a BB temperature of 53 C and 50% well fill, is 23 mK, as shown in Figure 7(d), where it is also plotted as a function of temperature. In this plot, a BLIP temperature of approximately 140 K can be identified as the point at which the NETD increases by a factor of $\sqrt{2}$ above its low temperature value. This temperature is consistent with the temperature at which the image quality in Figure 7(c) starts to degrade.

An important property of the gallium free detector is that the QE decreases strongly with temperature, so the integration time for the 80 K image in Figure 7(c) is significantly larger than that for the 120 K image. This is related to the fact that the minority carriers are localized and exhibit non-metallic hopping conductivity. The localization can be understood in terms of the Mott theory for the metal-insulator transition where the mini-band width in the ideal T2SL is narrower than typical energy fluctuations in the VB due, for example, to well width variations caused by interface steps of one or more monolayers [17, 3].

The lateral diffusion length, $L_{D||}$, can be determined by fitting the QE to the formula: $QE = QE_{\infty} \left(\frac{L+2L_{D||}}{L} \right)^2$, as shown schematically in Figure 8(a) for back illuminated test devices without an ARC, where L is the mesa side dimension and QE_{∞} is the quantum efficiency for $L \rightarrow \infty$. [18]. The diffusion length and QE decrease strongly with both increased doping and decreasing temperature, as shown by the curves in Figures 8(b) and 8(c). The reduction due to doping is related to the decrease in the minority carrier lifetime discussed above, while the effect of temperature is related to freezing out of the localized carriers. In Figure 8(c), QE values averaged over the BB spectrum are also shown as circles for FPAs fabricated from the same wafers and which include ARCs. The test devices were measured with a spectral band filter of 3.2-3.6 μ m while the filter used with the FPAs had a range of 3.6-5.1 μ m. This range is shown by the shaded region in Figure 8(d) which presents a comparison between the measured spectral response of the high doped FPA at 120 K and the response simulated with a vertical diffusion length of 1.5 μ m and the absorption spectrum calculated with the $\mathbf{k} \cdot \mathbf{p}$ model mentioned above. The wider band width for the FPAs tends to reduce the average QE compared with the test devices, because it has a stronger weighting from weaker absorption close to the cut-off wavelength, but the ARC increases the QE by about 40%, so the circles which show the FPA QE values in Figure 8(c) are fairly close to the curves for the test devices. The vertical diffusion length of 1.5 μ m at 120 K, which gave a good fit in Figure 8(d), is plotted as a blue circle in Figure 8(b) where it can be compared with the lateral value on the blue curve of 1.0 μ m. Vertical diffusion lengths are also included as red circles in this Figure for the low doped wafer at 80 K and 120 K, where again the vertical values are only slightly larger than the lateral values.

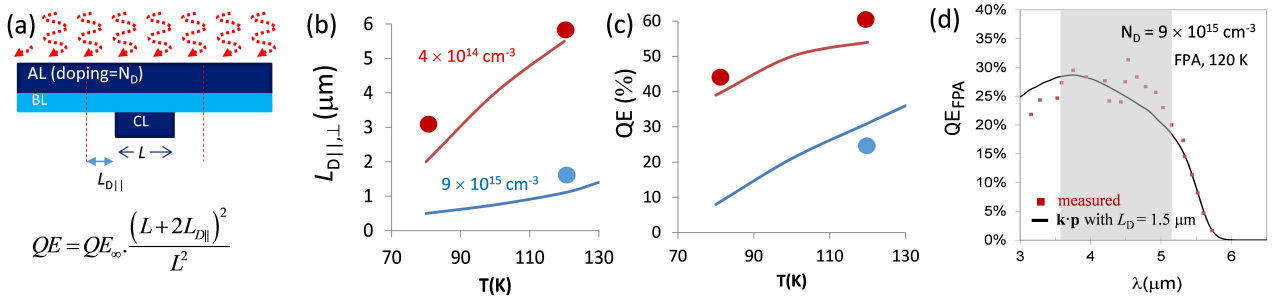


Figure 8. QE and diffusion length for the two InAs/InAs_{0.61}Sb_{0.39} T2SL nBn devices in Figure 7. (a) Method of measuring $L_{D||}$ and QE_{∞} using back illumination without an ARC. The curves in (b) and (c) show the results obtained with a BB spectral bandwidth (SB) of 3.2-3.6 μ m. The circles show $L_{D\perp}$ and QE deduced from FPAs with an ARC and a SB of 3.6-5.1 μ m. The SB is shown shaded in (d), where the spectral response measured at 120 K for the higher doping level is shown as points. The black curve shows the simulated spectral response based on a $\mathbf{k} \cdot \mathbf{p}$ model of the absorption spectrum and a vertical diffusion length of 1.5 μ m, corresponding to the blue circle in (b).

Based on the Einstein relation, $L_D = \sqrt{\frac{kT}{e}\mu\tau}$, the vertical diffusion lengths at 120 K for both high and low doped samples in Figure 8(b) are consistent with a mobility value of approximately $\mu = 3 \text{ cm}^2/\text{Vs}$ and the lifetimes deduced above from the dark current Arrhenius plots. This value of the mobility is about an order of magnitude smaller than in InAs/GaSb short period XB n devices [12]. In both cases the mean free path is less than a T2SL period and falls below the Ioffe-Regel limit for metallic transport [19], confirming the localized nature of hole minority carriers in T2SL materials and a hopping transport mechanism which freezes out at low temperatures [12].

An interesting feature of the diffusion results in Figure 8(b) is the isotropic nature of the diffusion. It was recently postulated that the diffusion might actually be rather anisotropic, due to hopping transport in the growth direction and metallic transport parallel to the layers. Such anisotropic diffusion could lead to strongly enhanced cross talk for pixels delineated with a shallow etch [20]. However, this turns out not to be the case and the electrical cross talk for the FPA in Figure 7 (c) is actually quite well behaved and virtually identical to that for a standard XB n FPA with a $4.2 \mu\text{m}$ cut-off and a similar pitch [21].

5. CONCLUSION

We have presented SCD's multi-faceted approach to the fabrication of HOT MWIR FPAs based on III-V materials. Using an epitaxial p - n junction the operating temperature of InSb photodiodes has been increased to $\sim 100 \text{ K}$. InSb has the advantage of very high image quality based on a highly uniform binary material with excellent crystal quality. However, even the epitaxial FPAs require fairly bulky Dewar and cooler assemblies compared with the miniaturization that is feasible in the 120-150 K range. This range has been attained using an XB n /XB p barrier device architecture, which strongly suppresses the G-R contribution to the dark current. InAsSb XB n devices grown lattice matched to a GaSb substrate have a cut-off wavelength of $4.2 \mu\text{m}$ and operate at 150 K with excellent image quality. The DDC assembly of SCD's $10 \mu\text{m}$ pitch 0.33 megapixel Sparrow detector has a maximum dimension of 62 mm, while the $5 \mu\text{m}$ pitch Crane detector with 5.24 megapixels has dimensions of just $88 \times 71 \times 68 \text{ mm}^3$. In both cases the power consumption is considerably reduced compared with InSb. These detectors operate in one of the most transparent atmospheric windows and in addition to many low SWaP applications, they are ideal for long range imaging and 24/7 surveillance.

In applications that require full MWIR coverage up to $\sim 4.9 \mu\text{m}$, we have explored several options including a direct derivative of the InAsSb XB n technology grown non-lattice matched on a buffer layer, and lattice matched T2SL based solutions. The exact solution for a given application depends on a trade-off between image quality, operating temperature and QE. The non-lattice matched device offers almost identical dark current and QE performance to MCT Rule 07, but image quality is quite sensitive to the conditions of crystal growth. In contrast T2SL FPAs are lattice matched to a GaSb substrate and image quality is less affected. InAs/GaSb XB p FPAs can operate close to 120 K with a QE above 50%. A similar operating temperature and a QE of above 60% has been demonstrated in gallium free InAs/InAs $_{0.61}$ Sb $_{0.39}$ FPAs. Doping close to $4 \times 10^{14} \text{ cm}^{-3}$ is used in the AL in order to suppress Auger recombination which can limit the lifetime and diffusion length. Although excellent HOT full MWIR performance is achieved, the QE tends to freeze out at low temperatures due to a hopping conduction mechanism for the minority carriers. This technology is therefore less suitable for incorporation in future dual band detectors which include a LWIR component operating at $\sim 80 \text{ K}$.

Prototype HFMW FPA detectors with a $15 \mu\text{m}$ pitch, a $\sim 4.9 \mu\text{m}$ cut-off wavelength and an operating temperature of $\sim 120 \text{ K}$ have already been delivered, and initial production is scheduled to begin by the middle of 2022.

ACKNOWLEDGMENTS

The authors acknowledge technical support from Mr. I. Bogoslavski, Mr. Y. Caracenti, Mr. A. Franco, Mr. M. Grinberg, Mr. S. Greenberg, Mr. D. Gur, Ms. N. Hazan, Ms. L. Krivolapov, Ms. M. Menahem, Ms. H. Moshe, Mr. Y. Osmo, Mr. E. Sandik, and Ms. H. Schanzer, who have all contributed to the successful growth, processing, packaging and characterization of the materials and devices.

REFERENCES

- [1] W. Shockley and W. Read *Phys. Rev.* **87**, p. 835, 1952.
- [2] R. Hall *Phys. Rev.* **87**, p. 387, 1952.
- [3] P. C. Klipstein *Appl. Phys. Lett.* **120**, p. 060502, 2022.
- [4] D. Reago, "Future army applications for infrared focal plane arrays," *Program of SPIE Defense and Security* **6940**(6940-82), 2008.
- [5] J. A. Lott, L. R. Dawson, E. D. Jones, and J. F. Klem *Appl. Phys. Lett.* **56**, p. 1242, 1990.
- [6] D. R. Fink, S. Lee, S. H. Kodati, V. Rogers, T. J. Ronningen, M. Winslow, C. H. Grein, A. H. Jones, J. C. Campbell, J. F. Klem, and S. Krishna *Appl. Phys. Lett.* **116**, p. 072103, 2020.
- [7] P. C. Klipstein, *Molecular Beam Epitaxy: Materials and Applications for Electronics and Optoelectronics*, ch. 15, p. 247. John Wiley and Sons Ltd., 2019.
- [8] L. Shkedy, E. Armon, E. Avnon, N. Ben Ari, M. Brumer, C. Jakobson, P. Klipstein, Y. Lury, O. Magen, B. Milgrom, T. Rosenstock, N. Shiloah, and I. Shtrichman *Proc. SPIE* **11741**, p. 117410W, 2021.
- [9] P. C. Klipstein, Y. Benny, Y. Cohen, N. Fraenkel, S. Glikzman, A. Glozman, I. Hirsh, L. Langof, I. Lukomsky, I. Marderfeld, B. Milgrom, M. Nitzani, D. Rakhmilevich, L. Shkedy, N. Snapi, I. Shtrichman, E. Weiss, and N. Yaron *J. Electr. Mater.* **49**, p. 6893, 2020.
- [10] W. E. Tennant *J. Electr. Mater.* **39**, p. 1030, 2010.
- [11] P. Klipstein, E. Avnon, Y. Benny, Y. Cohen, R. Fraenkel, S. Glikzman, A. Glozman, E. Hojman, O. Klin, L. Krasovitsky, L. Langof, I. Lukomsky, I. Marderfeld, N. Yaron, M. Nitzani, N. Rappaport, I. Shtrichman, N. Snapi, and E. Weiss *J. Electr. Mater.* **47**, p. 5725, 2018.
- [12] P. C. Klipstein, Y. Benny, Y. Cohen, N. Fraenkel, R. Fraenkel, S. Glikzman, A. Glozman, I. Hirsch, O. Klin, L. Langof, I. Lukomsky, I. Marderfeld, B. Milgrom, H. Nahor, M. Nitzani, D. Rakhmilevich, L. Shkedy, N. Snapi, I. Shtrichman, E. Weiss, and N. Yaron *Proc. SPIE* **11741**, p. 117410N, 2021.
- [13] E. H. Steenbergen, B. C. Connelly, G. D. Metcalfe, H. Shen, M. Wraback, D. Lubyshev, Y. Qiu, J. M. A. Fastenau, W. K. Liu, S. Elhamri, O. O. Cellek, and Y.-H. Zhang *Appl. Phys. Lett.* **99**, p. 251110, 2011.
- [14] Y. Aytac, B. V. Olson, J. K. Kim, E. A. Shaner, S. D. Hawkins, J. F. Klem, M. E. Flatté, and T. F. Boggess *Appl. Phys. Lett.* **105**, p. 022107, 2014.
- [15] E. A. Kadlec, B. V. Olson, M. D. Goldflam, J. K. Kim, J. F. Klem, S. D. Hawkins, W. T. Coon, M. A. Cavaliere, A. Tauke-Pedretti, T. R. C. Fortune, T. Harris, and E. A. Shaner *Appl. Phys. Lett.* **109**, p. 261105, 2016.
- [16] P. Klipstein, O. Klin, S. Grossman, I. Lukomsky, D. Aronov, M. Yassen, A. Glozman, T. Fishman, E. Berkowicz, O. Magen, I. Shtrichman, and E. Weiss *Optical Eng.* **50**, p. 061002, 2011.
- [17] N. F. Mott, *Metal-insulator transitions*, ch. 1, pp. 30–40. Taylor and Francis (London), 1974.
- [18] P. C. Klipstein, Y. Benny, S. Glikzman, A. Glozman, E. Hojman, O. Klin, L. Langof, I. Lukomsky, I. Marderfeld, M. Nitzani, N. Snapi, and E. Weiss *Infr. Phys. and Technol.* **96**, p. 155, 2019.
- [19] A. F. Ioffe and A. R. Regel, *Progress in Semiconductors*, vol. 4, ch. "Non-crystalline, amorphous and liquid semiconductors", p. 237. 1960.
- [20] J. Schuster *IEEE transactions on electronic devices* **66**, p. 1338, 2019.
- [21] P. Klipstein, Y. Gross, D. Aronov, M. ben Ezra, E. Berkowicz, Y. Cohen, R. Fraenkel, A. Glozman, S. Grossman, O. Klin, I. Lukomsky, T. Markowitz, L. Shkedy, I. Shtrichman, N. Snapi, A. Tuito, M. Yassen, and E. Weiss *Proc. SPIE* **8704**, p. 87041S, 2013.